Rotation sensing with trapped ions

2017 J. Phys. B: At. Mol. Opt. Phys. 50 064002

(http://iopscience.iop.org/0953-4075/50/6/064002)

IOP Publishing Journal of Physics B: Atomic, Molecular and Optical Physics
J. Phys. B: At. Mol. Opt. Phys. **50** (2017) 064002 (8pp) https://doi.org/10.1088/1361-6455/aa5a8f

Rotation sensing with trapped ions*

W C Campbell[1,2] **and P Hamilton**[1]

[1] UCLA Department of Physics and Astronomy, Los Angeles, CA 90095, United States of America
[2] California Institute for Quantum Emulation, Santa Barbara, CA 93106, United States of America

E-mail: wes@physics.ucla.edu

Received 31 August 2016, revised 11 December 2016
Accepted for publication 12 January 2017
Published 23 February 2017

Abstract

We present a protocol for rotation measurement via matter-wave Sagnac interferometry using trapped ions. The ion trap based interferometer encloses a large area in a compact apparatus through repeated round-trips in a Sagnac geometry. We show how a uniform magnetic field can be used to close the interferometer over a large dynamic range in rotation speed and measurement bandwidth without contrast loss. Since this technique does not require the ions to be confined in the Lamb–Dicke regime, Doppler laser cooling should be sufficient to reach a sensitivity of $\mathcal{S} = 1.4 \times 10^{-6}$ rad s^{-1} Hz$^{-1/2}$.

Keywords: atom interferometry, Sagnac, quantum metrology, gyroscope, trapped ion

(Some figures may appear in colour only in the online journal)

1. Introduction

The Sagnac effect can be used to measure the rotational velocity $\mathbf{\Omega}$ of a reference frame by observing the phase shift of an interferometer in that frame whose paths enclose an area A perpendicular to any component of $\mathbf{\Omega}$ (see, e.g. [1] for a review). The rotation-induced phase shift is given by

$$\Phi = 2\pi\frac{2E}{hc^2}\mathbf{A}\cdot\ \mathbf{\Omega}, \tag{1}$$

where $\mathbf{A}$ is the vector area enclosed by the two paths. E is the total energy of the particles that are interfering, defined using the relativistic energy–momentum relation

$$E^2 = (mc^2)^2 + p^2c^2. \tag{2}$$

For photons, $E = \hbar\omega_{\text{optical}}$, whereas for atoms of rest mass m moving at non-relativistic speeds ($p \ll mc$), $E = mc^2$.

The sensitivity of a gyroscope is defined as the minimum detectable rotation rate within a detection bandwidth Δf. For a shot-noise-limited interferometer that detects the outcome of individual interference events at a rate $\dot{N}$, the uncertainty in the measured phase after running for a time $t = 1/\Delta f$ will be $\delta\phi \approx \sqrt{\Delta f/\dot{N}}$. The sensitivity is given by

$$\mathcal{S} = \frac{\delta\phi}{\frac{\partial\Phi}{\partial\Omega}\sqrt{\Delta f}} = \frac{1}{\frac{\partial\Phi}{\partial\Omega}\sqrt{\dot{N}}}, \tag{3}$$

where the *scale factor* is given by

$$\frac{\partial\Phi}{\partial\Omega} = 2\pi A\frac{2E}{hc^2} \tag{4}$$

and we have assumed an orientation such that $\mathbf{A}\cdot\mathbf{\Omega} = A\Omega$ for algebraic simplicity.

The two methods frequently employed to improve the sensitivity of interferometric gyroscopes are increasing A and increasing E. For photons, optical fibers (or ring laser cavities) allow many effective round-trips through the Sagnac interferometer, thereby giving the device an effective area that is the physical area multiplied by 2 times the number of round trips (M). The other approach is to use atoms on ballistic trajectories instead of photons, which increases E by a factor of $mc^2/\hbar\omega_{\text{optical}} \approx 10^{11}$. Some of the drawbacks of this, as compared to aty 7n optical gyroscope, are that $\dot{N}$ is smaller, and the free-flight atom trajectories enclose the interferometer area A only once. The latter constraint has meant that increasing A has necessarily involved increasing the physical size of the apparatus, which can be undesirable for some applications. Furthermore, long atom trajectories and large separations make the measurement susceptible to systematics that can produce path-dependent phase shifts, such as magnetic field gradients.

Here, we show that trapped atomic ions provide a way to use both methods simultaneously to increase the interferometer

* This article belongs to the special issue: emerging leaders, which features invited work from the best early-career researchers working within the scope of *J. Phys.* B. This project is part of the *Journal of Physics* series' 50th anniversary celebrations in 2017. Wes Campbell was selected by the Editorial Board of *J. Phys.* B as an Emerging Leader.

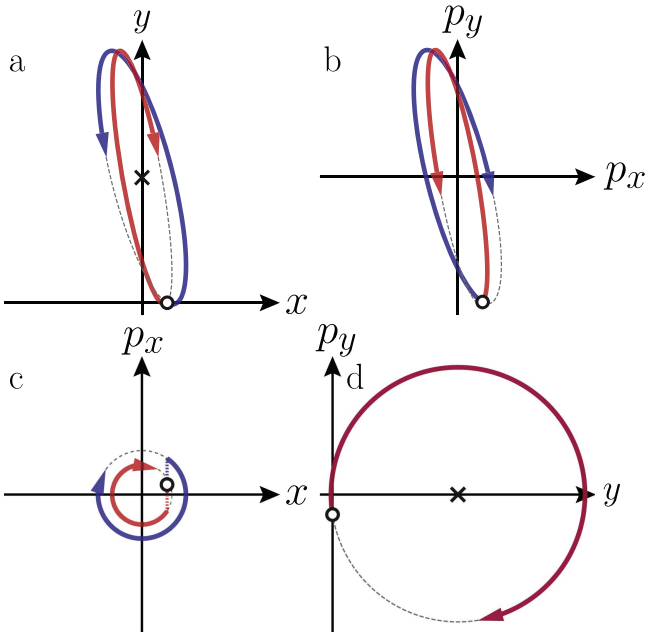

Figure 1. Trajectories of an ion during interferometer operation in (a) position space, (b) momentum space (c) x phase space and (d) y phase space. The ion's starting coordinates are indicated by a circle, and the trap center after the y-displacement in step (iii) is indicated by an $\times$. Red and blue curves represent the trajectory for the two spin states. Trajectories for different starting conditions are qualitatively similar to these, with the exception that for an ion cooled to the ground state of motion, the trajectories for the two spin states completely overlap.

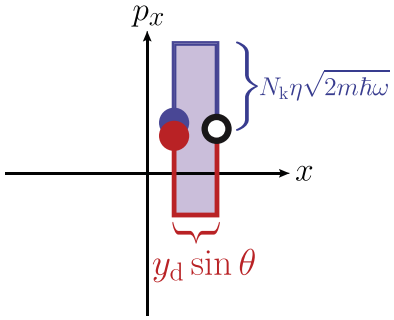

Figure 2. Trajectory of an ion in x phase space in the interaction picture with respect to the harmonic oscillation. The ion's starting coordinates are indicated by a circle, and red and blue curves represent the trajectory for the two spin states. A freely evolving coherent state in this 'rotating frame' (rotating in phase space, as opposed to real space) appears stationary; the trajectories shown are induced by the displacement operators. For small rotations ($\theta \ll 1$), the area enclosed in this phase space is the Sagnac phase (19) for an ion that starts at position $y = 0$.

sensitivity. While interferometers with enclosed area have been demonstrated with clouds of trapped neutral atoms [2, 3], maintaining the coherence across the ensemble needed for a gyroscope has proved difficult, and alternative ideas have been proposed [4, 5]. We describe a combination of laser-driven spin-dependent momentum kicks in one direction with ion trap voltage changes along an orthogonal direction that perform interferometry with trapped ions in a Sagnac (as opposed to Mach–Zehnder) configuration. Much like an optical gyroscope, this allows atomic trajectories to repeatedly enclose the same physical area, thereby accumulating Sagnac phase continuously for a time that is not limited by a ballistic flight trajectory. Since the enclosed area is proportional to the displacement along both directions and only one of these needs to be state-dependent, the interferometer area can be increased with trap voltage alone, circumventing the need to drive more coherent momentum transfer from the laser. The harmonic trapping potential makes the area enclosed independent of the initial ion velocity, eliminating a source of scale factor instability found in free space atom interferometers. These factors, coupled with the extremely long coherence times of trapped ions, give the trapped ion interferometer the potential to enclose a large effective area in a small apparatus with high stability.

2. Interferometer operation

We begin by introducing the protocol for measuring rotations with a single ion that hosts a qubit with internal states $|\uparrow\rangle$ and $|\downarrow\rangle$. As shown in figure 1, the enclosed area is in the x, y plane, and the (secular) trap frequencies for the ion in these two directions after the y displacement (see below) are degenerate: $\omega_x = \omega_y \equiv \omega$. (x, y, z) denote coordinates in real space, while (X, Y, Z) refer to axes of the qubit's associated Bloch sphere. The confinement in the z-direction is strong ($\omega_z \gg \omega$) so that the system can be approximated as being 2D. The time-sequence of the trapped ion gyroscope proceeds in the following steps (see also figures 1 and 2):

(i) Prepare the ion in $|\downarrow\rangle$ and apply a $\pi/2$ pulse of microwaves about $-\hat{\mathbf{Y}}$.
(ii) Apply N_k spin-dependent kicks (SDKs) in the x-direction ($\Delta\mathbf{p} = -N_k\hbar\Delta\mathbf{k}\hat{\sigma}_Z$) to separate the atom in momentum space.
(iii) Apply a step function in electrode voltages to non-adiabatically ($t \ll 2\pi/\omega$) displace the trap center in the y-direction a distance y_d.
(iv) Allow the ion to oscillate in the trap for an integer number (M) of round trips $\Delta t = M2\pi/\omega$.
(v) Reverse step (iii) by non-adiabatically switching the trap voltages back to their original values.
(vi) Reverse step (ii) by applying N_k SDKs in the other direction ($\Delta\mathbf{p} = N_k\hbar\Delta\mathbf{k}\hat{\sigma}_Z$) to close the interferometer.
(vii) Apply another $\pi/2$ pulse with microwaves about an axis inclined by ϕ in the X, Y plane from the $-\hat{\mathbf{Y}}$ axis of the Bloch sphere, then measure the internal state of the ion in the qubit basis.

Steps (i) and (vii) are a standard Ramsey sequence, therefore qubit and microwave oscillator coherence are required for the duration of the protocol. Even for non-clock-state qubits with magnetic sensitivity on the order of a Bohr magneton (μ_B), qubit coherence times of the order 1 s or greater have been achieved [6]. We will describe the details of the gyroscope protocol assuming the magnetic field on the ion is zero before discussing the magnetic field effects.

3. Phase–space displacements

The trapped ion gyroscope relies on two different methods to produce displacements in motional phase space: SDKs that transfer photon momenta to the ions in directions that depend upon the ion spin (qubit) state, and fast ($t \ll 2\pi/\omega$) trap voltage changes that rapidly displace the trap center. Since a displacement operation in phase space necessarily involves a large number of Fock states, both of these operations take place much faster than the resolved-sideband limit ($T_{\mathrm{rsl}} \approx 2\pi/\omega$) and therefore drive many number state transitions at once.

The first type of displacement operations, the SDKs [7] of steps (ii) and (vi), act as the beam splitters in the matter-wave interferometer. The speed of the SDK is enabled through the utilization of 'ultrafast' (mode-locked) lasers to transfer $\hbar\Delta k$ of momentum to the ion using time-dependent beat notes between counter-propagating laser beams (see [7, 8] for more detail). Conceptually, the ideal SDK transfers momentum to the ion whose direction is reversed for the two spin states via the operator

$$\hat{U}_{\mathrm{SDK}} = \hat{D}_x[\mathrm{i}\eta]\hat{\sigma}_+ + \hat{D}_x[-\mathrm{i}\eta]\hat{\sigma}_-, \tag{5}$$

where $\hat{D}_x[s]$ displaces a coherent state in x phase space a complex distance s (see figures 1 and 2) and η is the Lamb–Dicke factor for the laser-ion interaction in the x-direction ($\eta \equiv \Delta k x_0 = \Delta k\sqrt{\hbar/2\,m\omega}$). Since step (vi) drives the same process as (ii) with the direction of the kicks reversed (effectively replacing $\mathrm{i} \to -\mathrm{i}$ in (5)), we have suppressed the laser beat note phase when writing (5) since it plays no role as long as it is stable during a single enactment of the interferometer protocol. The qubit raising and lowering operators ($\hat{\sigma}_\pm$) flip the spin state of the qubit, so one way to make larger displacements (i.e. N_{k} individual SDKs) is by repeating this operation after a delay of half a motional period [9]. For algebraic simplicity, we will assume for our protocol that the number of SDKs applied (N_{k}) is even and that an extra half-period of motion is inserted after the last kick to preserve the harmonic oscillation phase of the initial motional state.

Working in the coherent state basis for describing the ion's motion in x and y (denoted by coherent state parameters α_x and α_y), step (i) results in the state

$$|\psi_{\mathrm{i}}\rangle = \tfrac{1}{\sqrt{2}}(|\downarrow\rangle + |\uparrow\rangle) \otimes |\alpha_x, \alpha_y\rangle. \tag{6}$$

The SDKs in step (ii) induce spin-motion coupling to produce the entangled state

$$|\psi_{\mathrm{ii}}\rangle = \tfrac{1}{\sqrt{2}}\Big(\mathrm{e}^{\mathrm{i}N_{\mathrm{k}}\eta\mathbb{R}(\alpha_x)}|\downarrow\rangle \otimes |\alpha_x + \mathrm{i}N_{\mathrm{k}}\eta\rangle + \mathrm{e}^{-\mathrm{i}N_{\mathrm{k}}\eta\mathbb{R}(\alpha_x)}|\uparrow\rangle \otimes |\alpha_x - \mathrm{i}N_{\mathrm{k}}\eta\rangle\Big) \otimes |\alpha_y\rangle, \tag{7}$$

where $\mathbb{R}(\alpha)$ denotes the real part of the coherent state parameter α.

Interferometers based on SDKs have been proposed [10] to measure the Sagnac effect, and have recently been implemented in a 1D non-Sagnac geometry to measure temperature over a wide dynamic range [9]. However, for a Sagnac gyroscope, the second displacement need not be spin-dependent and can therefore be implemented as a simple trap center shift. Electrode voltages can be rapidly changed to displace the trap center, an operation that has been demonstrated to couple to thousands of Fock states to perform a coherent state displacement operation [11]. Compared to coherent momentum transfer from a laser, voltage-driven motion of this sort can produce a larger displacement, and does so without the detrimental effects of spontaneous emission and differential AC Stark shifts associated with laser-driven gates.

A rapid shift of the trap center by a physical distance y_{d} along y can be modeled with a displacement operator

$$\hat{D}_y\Big[-\tfrac{y_{\mathrm{d}}}{2y_0}\Big]|\alpha_y\rangle = \Big|\,\alpha_y - \tfrac{y_{\mathrm{d}}}{2y_0}\Big\rangle, \tag{8}$$

where $y_0 = x_0 \equiv \sqrt{\hbar/2\,m\omega}$ and global phase terms are suppressed.

4. Rotation-induced phase

The effect of rotation in this system can be described in either the non-rotating frame (the ion frame) or the rotating reference frame (the apparatus frame). We choose the former, which means that the rotation manifests itself as change in the direction of the kicks between steps ((ii) and (iii)) and steps ((v) and (vi)). A constant rotation rate Ω about the positive z-axis of the apparatus will shift the angles of these kicks by

$$\theta = \Omega\Delta t = \Omega M\frac{2\pi}{\omega}. \tag{9}$$

This transforms the displacement operators according to

$$\hat{D}' = \mathrm{e}^{-\mathrm{i}\theta\hat{J}_z}\hat{D}\,\mathrm{e}^{\mathrm{i}\theta\hat{J}_z} \tag{10}$$

and the state of the ion after step (vi) is

$$\begin{aligned}|\psi_{\mathrm{vi}}\rangle = \tfrac{1}{\sqrt{2}}\Big(&\mathrm{e}^{\mathrm{i}\delta/2}|\downarrow\rangle \otimes \Big|\alpha_x + \mathrm{i}N_{\mathrm{k}}\eta(1-\cos\theta) - \tfrac{y_{\mathrm{d}}}{2x_0}\sin\theta\Big\rangle \\ &\otimes \Big|\,\alpha_y - \tfrac{y_{\mathrm{d}}}{2y_0}(1-\cos\theta) - \mathrm{i}N_{\mathrm{k}}\eta\sin\theta\Big\rangle \\ &+ \mathrm{e}^{-\mathrm{i}\delta/2}|\uparrow\rangle \otimes \Big|\alpha_x - \mathrm{i}N_{\mathrm{k}}\eta(1-\cos\theta) - \tfrac{y_{\mathrm{d}}}{2x_0}\sin\theta\Big\rangle \\ &\otimes \Big|\,\alpha_y - \tfrac{y_{\mathrm{d}}}{2y_0}(1-\cos\theta) + \mathrm{i}N_{\mathrm{k}}\eta\sin\theta\Big\rangle\Big),\end{aligned} \tag{11}$$

where the relative phase (δ) is given by

$$\begin{aligned}\delta = 2N_{\mathrm{k}}\eta\Big(&\tfrac{y_{\mathrm{d}}}{2x_0}(1+\cos\theta)\sin\theta + \tfrac{y_{\mathrm{d}}}{2y_0}(1-\cos\theta)\sin\theta \\ &+ \mathbb{R}(\alpha_x)(1-\cos\theta) - \mathbb{R}(\alpha_y)\sin\theta\Big).\end{aligned} \tag{12}$$

For a finite rotation rate, this protocol leaves residual entanglement between the spin and motion in both x and y. Using $|\mu_{i,\mathrm{f}}(\theta)\rangle$ to denote the final motional states in x and y for the parts of the wavefunction that are associated with spin state $i \in \{\uparrow,\downarrow\}$ in (11), the overlap is

$$\langle \mu_{\downarrow,\mathrm{f}}(\theta)|\mu_{\uparrow,\mathrm{f}}(\theta)\rangle = \mathrm{e}^{-2\left(2N_{\mathrm{k}}\eta \sin\frac{\theta}{2}\right)^2}\mathrm{e}^{-\mathrm{i}\delta'}, \tag{13}$$

where the first term comes from the imperfect state overlap (which is confined entirely to momentum space) and the second is a pure phase term called the *overlap phase* δ':

$$\delta' \equiv 2N_{\mathrm{k}}\eta(\mathbb{R}(\alpha_x)(1-\cos\theta) - \mathbb{R}(\alpha_y)\sin\theta). \tag{14}$$

Residual entanglement between spin and motion will reduce the contrast of the interferometer, and it is the sum of δ and δ' that contributes the phase shift that is measured using this protocol. However, as we show below, the phase shift that is measured is unaffected by the initial ion temperature, and the residual entanglement (i.e. imperfect motional state overlap) can be suppressed by applying an appropriate magnetic field.

5. Readout

In order to measure the rotation-induced phase ($\delta + \delta'$), step (vii) applies a second $\pi/2$ microwave pulse with a controllable phase shift ϕ, yielding

$$|\psi_{\mathrm{vii}}\rangle = \frac{1}{2}\Big(\mathrm{e}^{\mathrm{i}\delta/2}(\mathrm{e}^{-\mathrm{i}\phi}|\uparrow\rangle + |\downarrow\rangle) \otimes |\mu_{\downarrow,\mathrm{f}}(\theta)\rangle + \mathrm{e}^{-\mathrm{i}\delta/2}(|\uparrow\rangle - \mathrm{e}^{\mathrm{i}\phi}|\downarrow\rangle) \otimes |\mu_{\uparrow,\mathrm{f}}(\theta)\rangle\Big). \tag{15}$$

This step maps the motional phase onto the internal state of the ion, which would then measured using standard fluorescence techniques. The probability of measuring, for instance, spin up ($|\uparrow\rangle$) is given by

$$\mathcal{P}(\uparrow,\theta,\phi) = \int \mathrm{d}^2\alpha_x \mathrm{d}^2\alpha_y\, P(\alpha_x)P(\alpha_y)\langle\psi_{\mathrm{vii}}|\uparrow\rangle\langle\uparrow|\psi_{\mathrm{vii}}\rangle, \tag{16}$$

where

$$\langle\psi_{\mathrm{vii}}|\uparrow\rangle\langle\uparrow|\psi_{\mathrm{vii}}\rangle = \frac{1}{2} + \frac{1}{2}\mathrm{e}^{-2\left(2N_{\mathrm{k}}\eta\sin\frac{\theta}{2}\right)^2} \times \cos\left(\phi - \frac{A(\alpha_y)}{\pi x_0^2}\sin\theta - 4N_{\mathrm{k}}\eta x_0^2\,\mathbb{R}(\alpha_x)(1-\cos\theta)\right) \tag{17}$$

and $P(\alpha_j)$ is the Glauber–Sudarshan P-representation describing the (potentially mixed) initial motional state in the coherent state basis. $A(\alpha_y)$ is the classical, geometric area of the ellipse enclosed by the ion trajectories in the x, y plane, which depends upon the initial position in y via $y_i = 2y_0\mathbb{R}(\alpha_y)$:

$$A(\alpha_y) \equiv \pi\, 2x_0N_{\mathrm{k}}\eta\,(y_{\mathrm{d}} - 2y_0\mathbb{R}(\alpha_y)). \tag{18}$$

In the appendix, we show that a semiclassical derivation agrees with this quantum calculation. If we expand the argument of the cosine in (17) to first order in θ, we see that it simplifies to $\phi - \Phi$, where

$$\Phi = \frac{A(\alpha_y)}{\pi x_0^2}\theta = 2\pi\frac{2\,mc^2}{hc^2}(2MA(\alpha_y))\Omega. \tag{19}$$

This is identifiable as the Sagnac phase shift (1) with an effective area of $A_{\mathrm{eff}} = 2MA(\alpha_y)$ since the ion encloses the ellipse area $A(\alpha_y)$ twice each period for M periods. (19) also provides insight into the origin of the scale factor of this interferometer: the rotation angle θ is effectively 'amplified' by a gain factor of $A(\alpha_y)/\pi x_0^2$, the ratio of the enclosed area to the area of the ground-state wavefunction. This gain factor is the angular momentum of the ion's motion divided by $\hbar$, and the interferometer can therefore be thought of as a generalized atomic or nuclear spin gyroscope with a very large effective spin.

6. Finite temperature

For an ion that is pre-cooled to the motional ground state along y ($\alpha_y = 0$), (19) gives precisely the desired outcome (1) for the trapped ion gyroscope. For an ion that is initially in a thermal state with mean phonon occupation numbers $\bar{n}_x = \bar{n}_y \equiv \bar{n}$, (16) can be used to calculate the probability of measuring spin up:

$$\mathcal{P}(\uparrow,\theta,\phi) = \frac{1}{2} + \frac{1}{2}\mathrm{e}^{-\left(4N_{\mathrm{k}}\eta\sin\frac{\theta}{2}\right)^2(\bar{n}+\frac{1}{2})} \times \cos\left(\phi - \frac{A(0)}{\pi x_0^2}\sin\theta\right), \tag{20}$$

which is valid to all orders in θ. The effect of finite temperature is a reduction in the contrast of the interference, but it does not produce a phase shift of the signal. However, since the exponent in (20) is proportional to $\sin^2(\theta/2)$ and the Sagnac phase shift is proportional to $\sin(\theta)$, the free evolution time (Δt in (9)) can be chosen to satisfy

$$\sin^2\left(\frac{\theta}{2}\right) \ll 16N_{\mathrm{k}}^2\eta^2\left(\bar{n} + \frac{1}{2}\right) \tag{21}$$

and the interferometer can be operated at essentially full contrast, even at high temperature. There is therefore no requirement that the ion be cooled to the Lamb–Dicke regime, and as we estimate below, Doppler cooling should be sufficient for full-contrast operation.

7. Magnetic field effects

Since the ion is moving while it is accumulating rotation-induced phase, a nonzero magnetic field will give rise to a Lorentz force on the moving monopole. For a magnetic field in the z-direction, this will cause the ion's orbit to precess in the x, y plane, which will lead to a false rotation signal. Specifically, the magnetically induced rotation rate (Ω_{m}) can be found [12] by equating the Lorentz and Coriolis forces for a uniform, static magnetic field in the z-direction ($\mathbf{B} = B_z\hat{\mathbf{z}}$):

$$2\,m\Omega_{\mathrm{m}}(\mathbf{v}\times\hat{\mathbf{z}}) = eB_z(\mathbf{v}\times\hat{\mathbf{z}}). \tag{22}$$

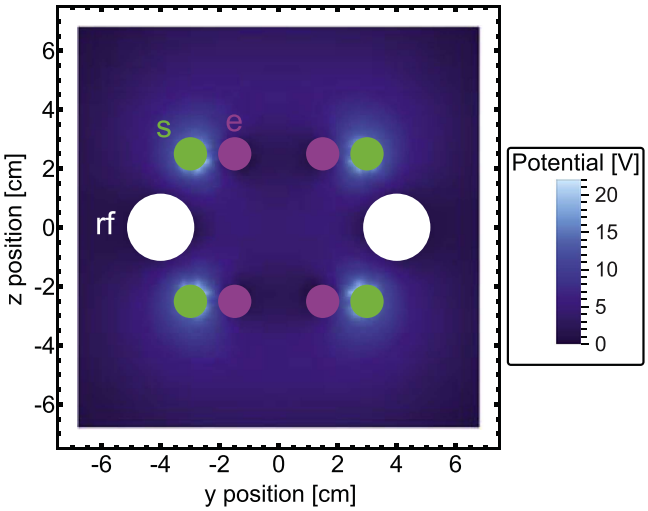

Figure 3. Numerical calculation (via finite element analysis) of the electric potential in an rf Paul trap designed for use as a gyroscope. The trap is rotationally symmetric about the $y = 0$ line in the figure, and consists of an rf ring ('rf', white), two DC end cap rings ('e', purple), and two DC shim rings ('s', green). The potential energy surface formed by putting rf voltage on the rf ring and positive DC voltage on the end caps will have a non-negligible quartic term, which can be shimmed out by putting a suitable DC voltage on the shim ring. This figure shows the calculated electric potential in the trap region from 22 V on the shim ring only. The coarseness of the finite element mesh is evident in the calculated potential, which can be used to estimate the effect of slight surface imperfections on real electrodes.

This rotation rate is half the cyclotron frequency $\omega_{\rm cyc} = eB/m = 2\Omega_{\rm m}$, and the precession angle this will produce is amplified by the gain factor of $A(0)/\pi x_0^2$ to give a magnetically induced phase shift of

$$\Phi_{\rm m} \equiv \Delta t\, \Omega_{\rm m} \frac{A(0)}{\pi x_0^2} = \Delta t \frac{2}{\hbar}\left(e\frac{\omega}{2\pi}\right)A(0)B_z. \tag{23}$$

This phase shift can be interpreted as the dynamical phase from the Zeeman shift of the ion's motional magnetic moment,

$$\mu_{\rm m} \equiv \frac{1}{2}\frac{\partial\left(\hbar\frac{\Phi_{\rm m}}{\Delta t}\right)}{\partial B_z} = IA(0), \tag{24}$$

where $I \equiv e\omega/2\pi$ is the current from the ion's motion. This matches the classical expression for the magnetic moment of a current loop of area $A(0)$. In section 11, we outline a practical implementation where this amounts to magnetic sensitivity of order $1\mu_{\rm B}$, a level that has been demonstrated to allow coherence times of greater than 1 s [6] with shielding.

8. Non-harmonic corrections

The analysis we have presented has thus far assumed a perfectly harmonic potential. We can find the first-order phase correction for small non-harmonic terms of the potential by treating these terms as a perturbation and integrating over the unperturbed trajectories. Assuming the potential remains separable the formulas below hold for each axis. Let us write the general potential as

$$V = \frac{1}{2}m\omega^2 x_l^2\left(\frac{x^2}{x_l^2} + C_3\frac{x^3}{x_l^3} + C_4\frac{x^4}{x_l^4} + \cdots\right), \tag{25}$$

where x_l is the amplitude of the ion's motion and the $\{C_i\}$ are dimensionless numbers assumed to be much smaller than one. With a harmonic trajectory $x(t) = x_l \sin(\omega t + \phi)$, only even i terms contribute non-zero phase shifts. Integrating over M orbits gives

$$\Delta\phi = \frac{1}{\hbar}\int_0^{2\pi M/\omega} {\rm d}t\, \frac{1}{2}m\omega^2 x_l^2 \sum_{i\geqslant 3} C_i \sin^i(\omega t + \phi) \tag{26}$$

$$= m\omega x_l^2 \frac{3\pi M}{8\hbar} C_4 + \cdots. \tag{27}$$

To estimate how stringent a requirement this will be on feasible ion traps, we have calculated this correction term for an example trap, shown in figure 3. The trap potential is made primarily through the pondermotive potential provided by putting a 50 kHz $= \Omega_{\rm rf}/2\pi$ sinusoidal voltage on the rf ring and the electric potential from positive DC voltages on the end cap rings. The quartic contribution to the overall potential from this arrangement is due almost entirely to the pondermotive part, and can then be canceled by putting DC voltage on the shim rings. Finite element analysis of the resulting potentials suggests that with an rf amplitude of 48 V, the quartic term in the x, y plane can be canceled by a voltage near 22 V of DC on the shim rings. The resulting trap will have a secular frequency of $\omega/2\pi = 10$ kHz in the x, y plane and the DC voltage on the end cap rings can be used to tune this frequency and confine the ions in the z-direction, possibly with slight additional shimming of the quartic term in the x, y plane. For the operating parameters we estimate below in section 11 ($N_{\rm k} = 100$, $M = 100$ round trips with $y_{\rm d} = 100\mu$m), the DC voltage control needed for the shim ring to keep $\Delta\phi < 0.1$ rad from (27) is at the level of $\approx$0.1 mV.

9. Requirements on the secular frequency

The experimental control needed to ensure sufficient stability and degeneracy of the secular frequencies in the x and y directions can also likewise be estimated for this example implementation (see figure 3). If the timing of step (v) or step (vi) is imperfectly matched to an integer number of oscillations, there will not be a phase shift (assuming a thermal state for the ion's initial motion), but there will be a reduction in the interference contrast.

We can model this as arising entirely from an error in the secular frequency that shifts it from ω to $\omega + \delta\omega$, where $M \equiv \Delta t\, \omega/2\pi$. For our estimated operating parameters (see section 11), the interference contrast will be reduced by a factor of 2 for $\delta\omega/\omega \approx 10^{-7}$. Ion secular frequencies in the comparatively high frequency and high voltage rf Paul traps used for quantum information processing have been stabilized at the 10^{-5} level [13]. We anticipate that ensuring

stability of the secular oscillations will be significantly easier in a low-voltage (≈50 V) trap driven at 50 kHz $= \Omega_{\rm rf}/2\pi$, where there will be no need for a resonant circuit and direct, real time measurement of the trap voltage waveform can be used for feedback stabilization. Cooling to the motional ground state before operation would relax this constraint to about 1 part in 3×10^5.

Ensuring degeneracy of the x and y secular frequencies is subject to essentially the same constraint above, where a mismatch between ω_x and ω_y can be made to look like a timing error in one or the other. The finite element analysis shown in figure 3 was done for end cap rings that are sectioned into four angular quadrants with submillimeter gaps between them to provide the ability to separately tune ω_x and ω_y. By using DC potentials on these, the trap frequencies in the x and y directions can be tuned to achieve the necessary level of degeneracy through DC quadrupole fields. Assuming that the mismatch between ω_x and ω_y is fixed, the voltage control necessary for the segmented end caps to achieve this is around the 50 μV level. It may be necessary to section the shim rings into quadrants as well if the residual quartic terms are significantly mismatched. Corrections for both the quartic terms and potential trap anisotropy are therefore confined to the DC electrodes, which are likely easier to adjust than tuning rf parameters.

10. Micromotion

Since we envision using an rf Paul trap for the trapped ion gyroscope, the rf micromotion in such a trap has the potential to introduce some complications. For a rotationally symmetric trap such as that shown in figure 3, the free-evolution (step (iv)) can be centered on the rf null, in which case the micromotion will be purely radial. Since this produces no torque on the orbit, it does not change the orbital angular momentum of the ion and, as we show in the appendix, fixed angular momentum means this will not change the effective enclosed area.

While having the correct timing and compensation of the trap will ensure that the secular motion of the ion wavepackets close, the true Matheiu trajectories are not guaranteed to close. It was for this reason that micromotion fringes are visible in the interferometry work of [7], and we envision operating the trapped ion gyroscope in a mode where the rf drive frequency is an integer multiple of ω and the experiment is triggered on on a fixed phase of the rf. The ease of doing this in the kHz regime instead of the MHz regime is one of the many advantages of working with a low-frequency trap.

11. Performance

Once the evolution time has been fixed, the sensitivity of the trapped ion gyroscope can be written

$$\mathcal{S} = \frac{1}{2N_{\rm k}\Delta k\ y_{\rm d}\sqrt{\Delta t}}. \tag{28}$$

Since this is independent of the trap frequency ω (we assume $M \gg 1$ and can therefore be chosen to achieve any desired value of Δt), the trapped ion gyroscope can be operated in a relatively low-frequency trap as compared to typical traps for applications requiring resolved sideband operations. This provides the practical advantage of making the non-adiabatic operations easier to achieve with high fidelity in a fixed time. It also permits the use of a trap whose electrodes are far apart and far from the ion, which will suppress surface-induced heating and patch charge perturbations as well as improve harmonicity for a fixed absolute length scale.

We also note that the performance of this rotation sensor is independent of the mass of the ion, and depends essentially only on the wavelength of the laser used to drive the SDKs. We will estimate parameters for $^{171}Yb^+$, which was used for the first demonstrations of SDKs [7], but estimates for other species will be similar in magnitude.

For the hyperfine clock-state qubit in $^{171}Yb^+$, stimulated Raman transitions can be driven by a tripled vanadate laser at $4\pi/\Delta k = 355$ nm [14] with $N_{\rm k} = 100$ [15]. Since this qubit has a demonstrated coherence time exceeding 1000 s [16], a free-evolution time of $\Delta t > 1$ s should be possible. For a (secular) trap frequency of $\omega/2\pi = 10$ kHz, a trap displacement of $y_{\rm d} = 100\ \mu$m would correspond to $\langle n\rangle \approx 9 \times 10^5$ phonons, where displacements corresponding to $\langle n\rangle \approx 10^4$ have already been demonstrated [11]. Cooling Yb^+ to the Doppler limit ($T_{\rm D} = \hbar\gamma/2k_{\rm B}$) in such a trap will result in an interference contrast of 85% for the (sidereal) rotation rate of the Earth $\Omega_{\rm e} \approx 73\ \mu$rad s^{-1}. A trapped ion gyroscope operated with these parameters would have a scale factor of $\partial\Phi/\partial\Omega = 52\ {\rm rad}/\Omega_{\rm e}/\sqrt{\rm s}$ and a sensitivity of $\mathcal{S} = 1.4 \times 10^{-6}$ rad s^{-1} Hz$^{-1/2}$. For $M = 100$ orbits during free-evolution, this corresponds to a scale factor of $\partial\Phi/\partial\Omega = 5.2\ {\rm rad}/\Omega_{\rm e}$. Improvements in the numbers of SDKs or the distance of coherent trap displacements would make this competitive with cold atom interferometers that use large numbers of atoms.

For an interferometer using the parameters discussed above, the magnetically induced rotation rate per unit field is $\Omega_{\rm m}/(2\pi B_z) = 4.5$ Hz G^{-1}. The associated motional magnetic moment is $\mu_{\rm m} = 1.1\ \mu_{\rm B}$, where $\mu_{\rm B}$ is the Bohr magneton. Since the magnetic field stabilization required to combat this systematic only needs to be applied to a small volume ($\ll 1$ cm^3), this magnetic sensitivity resembles the effect of using a Zeeman-sensitive qubit, and many of the technical difficulties associated with this have been overcome in various trapped ion quantum information processing experiments [6]. An alternative approach to mitigating this effect would be to intentionally choose a Zeeman-sensitive qubit with precisely the opposite sign for its magnetic moment. This is analogous to atomic states where the spin magnetic moment cancels the orbital magnetic moment while retaining finite total angular momentum, such as in the $^5F_1$ ground state of ruthenium.

In the limit where the magnetically induced rotation rate is much slower than the (secular) trap frequency ($\Omega_{\rm m} \ll \omega$), the ion moves in elliptical orbits of fixed area whose

orientation slowly rotates. Too much rotation will reduce the contrast of the interference signal since the kicks in step (v) and (vi) will not efficiently close the interferometer loop. However, trapped ions have also been demonstrated as superb magnetic field sensors, and it seems likely that with a periodic measurement of a stationary ion's Zeeman splitting, a well-controlled field could be applied to cancel this effect.

Likewise, magnetic rotation could be leveraged to cancel the contrast reduction associated with high actual rotation rates (the exponential factor in (17)). In this 'closed-loop mode', the magnetic field needed to cancel the rotation would become the output signal for the interferometer, and low-resolution rotation sensors could be incorporated to feed forward the magnetic field needed to keep the interferometer contrast maximized and on the steepest part of a fringe.

12. Discussion

The most sensitive large area laser ring gyroscope has a reported sensitivity of $\mathcal{S} = 1.2 \times 10^{-11}\,\mathrm{rad\,s^{-1}\,Hz^{-1/2}}$, achieved by enclosing a physical single-pass area of 16 $\mathrm{m^2}$ [17]. While the first-generation sensitivity of the trapped ion gyroscope we describe here does not project to be competitive with large area laser ring gyros, it is likely to find more utility in situations such as navigation, where the development of physically smaller devices is active [18]. The state of the art commercial navigation laser gyroscope is specified with a typical sensitivity of $\mathcal{S} = 10^{-6}\,\mathrm{rad\,s^{-1}\,Hz^{-1/2}}$ [19]. This is essentially the same as our projection for the ion system, and improvements beyond the first generation of this scheme may one day be able to surpass these commercial devices.

Free-flight matter-wave interferometers have demonstrated state of the art short term sensitivities of $\mathcal{S} = 6 \times 10^{-10}\,\mathrm{rad\,s^{-1}\,Hz^{-1/2}}$ for atomic beams [20] and $\mathcal{S} = 1 \times 10^{-7}\,\mathrm{rad\,s^{-1}\,Hz^{-1/2}}$ for laser-cooled atoms [21], which can provide better long-term stability than the atomic beam methods.

These short-term sensitivities for the neutral atom devices are better than our projected first generation sensitivity. However, the trapped ion gyroscope again provides some potential practical advantages as compared to these established, neutral atom techniques. First, the physical size of the interferometer can be compact while still retaining a large effective interferometer area by using multiple orbits. Second, since the ion wavepacket re-combines in space twice per trap period, this interferometer can be interrogated over a wide dynamic range of free-evolution times. Fast rotation rates, which can be problematic in neutral atom systems if the wavepackets either do not re-combine or leave the interferometry region, can be compensated by applying uniform magnetic fields. The operational mode could be to actively stabilize the fringes with an applied field, which becomes the readout signal. There is also no need to keep multiple optical beam paths interferometrically (relatively) stable since the only steps that are sensitive to a laser phase (the SDKs, steps (ii) and (vi)) are driven by the same laser with its beam traversing the same optical path. In addition, by using single ion wavepackets that travel the same average trajectory, only in opposite directions, we eliminate a class of spatially varying systematics. Finally, free-flight interferometers have sensitivities to accelerations and the atomic beam velocities, whereas the scale factor for the ion trap interferometer depends only on the momentum kicks and trap displacement.

Another advantage of using trapped ions instead of neutral atoms for matter-wave interferometry is the potential to leverage the advances in trapped ion quantum information processing to produce sub-shot-noise scaling of the sensitivity with ion number. For example, a collection of N_I ions could be prepared in step (i) in a GHZ [22] spin state

$$|\psi\rangle = \frac{1}{\sqrt{N_\mathrm{I}}}(|\downarrow\downarrow\downarrow\cdots\downarrow\rangle + |\uparrow\uparrow\uparrow\cdots\uparrow\rangle) \tag{29}$$

and the same protocol could be used as for the single ion to accumulate phase, but with the resolution (and sensitivity) enhanced by a factor of N_I. These states (29) have been created for as many as $N_\mathrm{I} = 14$ ions [23], and multiple groups are actively pursuing various ways to scale up the size of entangled trapped ion systems.

Acknowledgments

We thank Amar Vutha, Chris Monroe, Dana Anderson, Kale Johnson, Remi Geiger, and Eric Hudson for helpful discussions. WCC acknowledges support from the US Army Research Office under award W911NF-15-1-0261 and University of California Office of the President's Research Catalyst Award No. CA-15-327861. PH acknowledges support from the University of California Office of the President's Research Catalyst Award No. CA-16-377655.

Appendix. Area formula

We show using semiclassical derivation that the area enclosed by the interferometer is insensitive to the ion's initial position and momentum in x and initial momentum in y. Choosing a coordinate system centered on the trap center, the area enclosed by a periodic trajectory $\mathbf{r}(t)$ is given by the path integral

$$\mathbf{A} = \frac{1}{2}\oint \mathbf{r} \times \mathrm{d}\mathbf{r} = \frac{1}{2}\int_0^T \mathrm{d}t\ \mathbf{r}(t) \times \mathbf{v}(t) \tag{A.1}$$

$$= \frac{1}{2m}\int_0^T \mathrm{d}t\ \mathbf{J} = \frac{\mathbf{J}\,T}{2m}, \tag{A.2}$$

where $T \equiv 2\pi/\omega$ is the period and $\mathbf{J}$ is the angular momentum about the center of the trap. A momentum kick, $\Delta\mathbf{p}$, at the start of the trajectory (and taken to be along x) changes the angular momentum by $\Delta\mathbf{J}_\mathrm{SDK} = \mathbf{r}(0) \times \Delta\mathbf{p} = \mathbf{r}_\perp(0) \times \Delta\mathbf{p}$, where $\mathbf{r}_\perp(0)$ is the component of the initial displacement perpendicular to the direction of the momentum kick (which we will take to be the y-direction). The trap displacement in y then changes the angular momentum by $\Delta\mathbf{J}_\mathrm{d} = -y_\mathrm{d}\hat{\mathbf{y}} \times \mathbf{p}(0)$. We are interested in the areas for two trajectories with initial momentum kicks, $\pm\Delta\mathbf{p} = \pm N_\mathrm{k}\hbar\Delta k\hat{\mathbf{x}}$, in opposite directions

in x. The area enclosed by the interferometer is the difference between these areas, taken over half a motional period (since the interferometer closes at time $T/2$):

$$A = \left| \frac{\Delta \mathbf{J}\,\frac{T}{2}}{2m} \right| = \pi \frac{\Delta p}{m\omega}(y_{\mathrm{d}} - r_{\perp}(0)), \tag{A.3}$$

which agrees with (18). We see that the area difference depends only on the initial displacement perpendicular to the SDK direction and the size of the kick. The formula holds for circular, elliptical, or even straight line trajectories and is also independent of the initial momentum of the particle.

References

[1] Barrett B, Geiger R, Dutta I, Maunier M, Canuel B, Gauguet A, Bouyer P and Landragin A 2014 *C. R. Phys.* **15** 875

[2] Burke J H T and Sackett C A 2009 *Phys. Rev.* A **80** 061603(R)

[3] Wu S, Su E and Prentiss M 2007 *Phys. Rev. Lett.* **99** 173201

[4] Stevenson R, Hush M R, Bishop T, Lesanovsky I and Fernholz T 2015 *Phys. Rev. Lett.* **115** 163001

[5] Garrido Alzar C L, Yan W and Landragin A 2012 Towards high sensitivity rotation sensing using an atom chip *Research in Optical Sciences* (Washington, DC: Optical Society of America) Paper JT2A.10 (https://doi.org/10.1364/HILAS.2012.JT2A.10)

[6] Ruster T, Schmiegelow C T, Kaufmann H, Warschburger C, Schmidt-Kaler F and Poschinger U G 2016 *Appl. Phys.* B **122** 254

[7] Mizrahi J, Senko C, Neyenhuis B, Johnson K G, Campbell W C, Conover C W S and Monroe C 2013 *Phys. Rev. Lett.* **110** 203001

[8] Mizrahi J, Neyenhuis B, Johnson K G, Campbell W C, Senko C, Hayes D and Monroe C 2014 *Appl. Phys.* B **114** 45

[9] Johnson K G, Neyenhuis B, Mizrahi J, Wong-Campos J D and Monroe C 2015 *Phys. Rev. Lett.* **115** 213001

[10] Poyatos J F, Cirac J I, Blatt R and Zoller P 1996 *Phys. Rev.* A **54** 1532

[11] Alonso J, Leupold F M, Solèr Z U, Fadel M, Marinelli M, Keitch B C, Negnevitsky V and Home J P 2016 *Nat. Commun.* **7** 11243

[12] Sakurai J J 1980 *Phys. Rev.* D **21** 2993

[13] Johnson K G, Wong-Campos J D, Restelli A, Landsman K A, Neyenhuis B, Mizrahi J and Monroe C 2016 *Rev. Sci. Instrum.* **87** 053110

[14] Campbell W C, Mizrahi J, Quraishi Q, Senko C, Hayes D, Hucul D, Matsukevich D N, Maunz P and Monroe C 2010 *Phys. Rev. Lett.* **105** 090502

[15] Johnson K G, Wong-Campos J D, Neyenhuis B, Mizrahi J and Monroe C 2017 Ultrafast creation of large 'Schrödinger cat' states of an atom arXiv:1612.05854v2

[16] Fisk P T H, Sellars M J, Lawn M A and Coles C 1997 *IEEE Trans. Ultrason. Ferroelectr. Freq. Control* **44** 344

[17] Schreiber K U and Wells J P R 2013 *Rev. Sci. Instrum.* **84** 041101

[18] Ajoy A and Cappellaro P 2012 *Phys. Rev.* A **86** 062104

[19] Honeywell Phoenix A Z 2012 GG1320AN Digital Ring Laser Gyro

[20] Gustavson T L, Landragin A and Kasevish M A 2000 *Class. Quantum Grav.* **17** 2385

[21] Dutta I, Savoie D, Fang B, Venon B, Garrido Alzar C L, Geiger R and Landragin A 2016 *Phys. Rev. Lett.* **116** 183003

[22] Greenberger D M, Horne M A and Zeilinger A 1989 *Bell's Theorem, Quantum Theory, and Conceptions of the Universe* ed M Kafatos (Dordrecht: Kluwer) pp 73–6

[23] Monz T, Schindler P, Barreiro J T, Chwalla M, Nigg D, Cornish W A, Harlander M, Hänsel W, Hennrich M and Blatt R 2011 *Phys. Rev. Lett.* **106** 130506